



Full Length Article

Rotation induced by non-uniform gas–solid phase reactions of a non-spherical particle

Shengyu Zhou^{a,b}, Zhongjie Shen^{a,b}, Qinfeng Liang^{a,b}, Jianliang Xu^{a,b,*}, Zhenghua Dai^{a,b}, Haifeng Liu^{a,b,*}

^a Shanghai Engineering Research Center of Coal Gasification, East China University of Science and Technology, P. O. Box 272, Shanghai 200237, PR China

^b National Energy Coal Gasification Technology Research and Development Center, East China University of Science and Technology, P. O. Box 272, Shanghai 200237, PR China



ARTICLE INFO

Keywords:

Rotation
Induced thrust
Gas–solid phase reaction
Non-spherical particle
Active sites distribution

ABSTRACT

Particle rotation plays an important role in gas–solid flow. The particle rotation induced by gas–solid phase reaction is investigated in this work. The non-uniform gas–solid phase reaction directly results in the rotation of a non-spherical particle. Based on the random distribution of active sites, the combustion of non-spherical particles is numerically investigated. According to the numerical results of chemical reaction rate on the particle surface, the net force and the rotation frequency of non-spherical particles were obtained by post-processing. The bearing force and rotation of cubic particles caused by gas–solid chemical reactions are systematically numerically studied. The rotational frequency is basically consistent with the experimental results in the reference. For coal char particles with an active area ratio of 0.8, the rotational frequency can reach 1000 Hz at a side length of 60 μm. The effects of active area ratio, ambient gas temperature and particle size on the induced thrust and the rotational frequency of coal char particles are analyzed. The unbalanced force on the particle surface increases with the reaction rates. The rotation velocity increases with the decrease of particle size. And it increases with the increase of ambient temperature.

1. Introduction

The gas–solid non-catalytic reactions are widely used in chemical production processes, such as combustion [1–3]/gasification [4] of coal, the reduction of iron ore [5], and the decomposition/oxidation of pyrite [6–8]. In addition, the regeneration of catalysts deactivated by coke deposition also includes the gas–solid oxidation/reduction reactions [9,10]. The operation performance of these chemical productions is largely determined by the reaction and movement characteristics of solid particles. The force balance and more complex conservation of angular momentum of a single particle in the reaction process is of great concern to understand its effects on fluid dynamics in multi-phase flow. The rotation of particles is obtained from the conservation of angular momentum. The particle rotation affects the motion characteristics of particles [11] and turbulence modulation in gas–solid flow [12]. For coal gasification, the rotation of pulverized coal can avoid its linear trajectory in the gasifier, increasing the residence time and improving the carbon conversion. Under high rotation velocities, the centrifugal

force of pulverized coal particles leads to the crushing of coal and the shedding of ash [13,14]. In addition, the particle rotation affects heat transfer in entrained flow gasifiers, and it tends to decrease the non-uniformity of the temperature distribution [15]. Particles rotation is closely related to gas–solid reactions and flow.

The rapid rotation of particles was obviously observed in many visualization studies, like ignition and combustion characteristics study of pulverized coal and coal-water fuel aggregates [16–18]. The periodic variation of particle projection area and particle size in the combustion process reflected the rotation phenomenon of individual particles. And the rotation velocities were recorded. The rotational frequency was directly related to the reaction rate, which was determined by the furnace gas temperature, the oxygen partial pressure, and the particle size [19]. The rotation behavior of particles was usually attributed to the reaction force induced by volatile matter ejection from pores [19]. However, for anthracite particles with only 3.6% volatile matter, a very obvious rotation motion with a rotational frequency of 400 Hz has also been detected [16]. At the same time, particles have shown notable

* Corresponding authors at: National Energy Coal Gasification Technology Research and Development Center, East China University of Science and Technology, P. O. Box 272, Shanghai 200237, PR China.

E-mail addresses: xujl@ecust.edu.cn (J. Xu), hfliu@ecust.edu.cn (H. Liu).

<https://doi.org/10.1016/j.fuel.2022.125009>

Received 29 December 2021; Received in revised form 10 May 2022; Accepted 21 June 2022

Available online 5 July 2022

0016-2361/© 2022 Elsevier Ltd. All rights reserved.

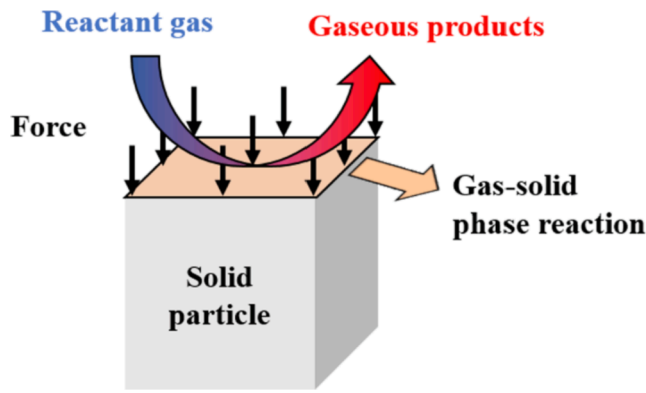


Fig. 1. The generating process of thrusts due to the gas–solid surface reactions.

continuous rotating phenomena during all combustion stages including volatile combustion, particle heat-up and char reaction processes [18]. Therefore, in addition to the ejection of volatile matter, the rotation mechanism induced by reactions is worthy of further study, especially for the rotation of anthracite particles and the continuous rotation in the char reaction process.

Our research group has observed and investigated the fluctuating motions of petroleum coke particles with low ash and volatile contents in the experimental process of combustion and gasification [20]. It was found that the non-uniformity distribution of active site on particle surface and structural irregularity account for the particle motion induced by gas–solid phase reactions. Coal contains complex organic materials and inorganic materials. The reactivity of coal was considered to be proportional to the number of active sites in the coal [21]. The formation of coal surface active sites [22–25] determined that the reactivity of single coal char varies with different micro areas. Each active micro area on the particle surface reacts and releases gaseous products to induce a reaction force [20] perpendicular to the micro surface, forming a net force on the whole particle. When the coal char particle is not a sphere, all the force components on the micro area of particle form a net torque, making the particle to rotate.

In this study, we investigated the rotation characteristics of a single non-spherical particle with gas–solid reactions. The reaction model of cubic coal char particles was established based on the random distribution of particle surface active sites. The fundamental mechanism of coal char particle rotation in the reaction process has been analyzed. And we studied the effects of active area ratio, ambient temperature and particle size on the induced thrust and rotation characteristic of reacting

coal char particles.

2. Particle rotation

2.1. Particle rotation mechanism

For the gas–solid surface reaction, the reactant gas diffuses from the surrounding to the surface of solid particles. Then the heterogeneous reactions occur on the particle surface to generate gaseous products, which are released outward. The absorption of reactants and the release of products both contribute to the impulses of force, forming the induced thrusts directed toward the interior of the particles at the reaction surface, as shown in Fig. 1. The thrusts at micro areas are directly related to the reactions rate. When the surface reactivity of a symmetrical solid particle is the same, the resultant force of these induced thrusts at particle surface is 0. However, for some solid particles whose surface reactivity changes with micro areas, such as coal, the net induced thrust formed by the gas–solid surface reactions depend on the reactivity of the micro-areas.

The complexity of coal composition results in non-uniform distribution of active sites on the particle surface [21]. As illustrated in Fig. 2 (A), the active sites are non-uniform distributed on the surface, where red represents the active surface and blue represents the non-active surface. The gas–solid surface reactions occur on active surface, and the gaseous products are released, forming a thrust F_i , perpendicular to the particle surface inward. Integrate the thrusts on the whole particle surface:

$$\sum F_i > 0$$

Therefore, for solid particles with non-uniform surface reactivity, the gas–solid surface reactions induce a non-zero resultant force.

For spherical particles, the normal directions of the micro areas on particle surface all cross the centroid of the sphere, resulting in the translation of particle. For non-spherical solid particles, the thrust magnitude and its direction on the particle surface are illustrated in Fig. 2(A). Thus, the torque of the force system on the non-spherical particle surface to the centroid O is expressed as:

$$M_O(\vec{F}_R) = \sum M_O(\vec{F}_i) > 0$$

For the solid particle in Fig. 2(A), a clockwise rotation moment M_O is obtained. Thus, for non-spherical particles with un-uniform surface reactivity, the gas–solid surface reactions lead to a non-zero resultant moment. The solid particle is rotated under this torque. The rotational angular acceleration and angular velocity are obtained. The particle

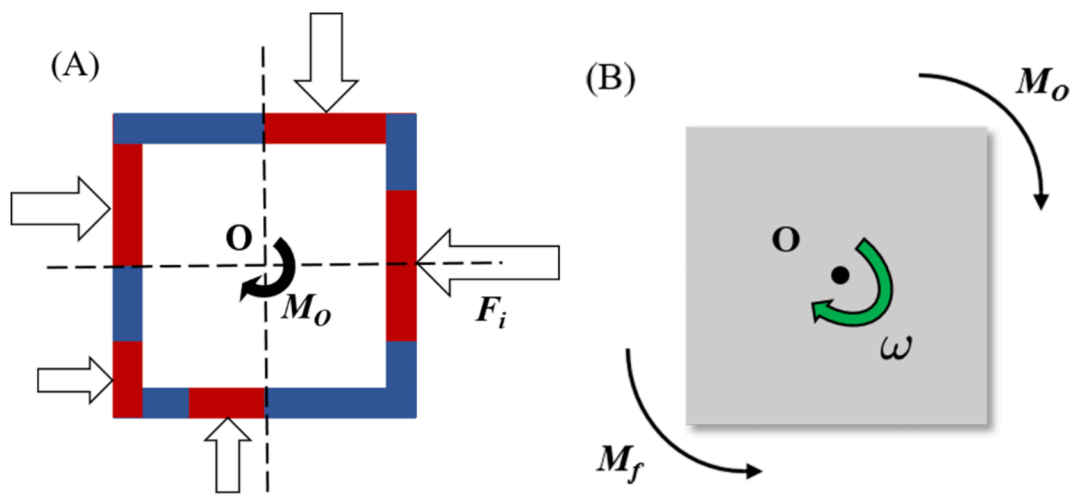


Fig. 2. (A) Formation and (B) balance of the torque M_O induced by gas–solid surface reactions.

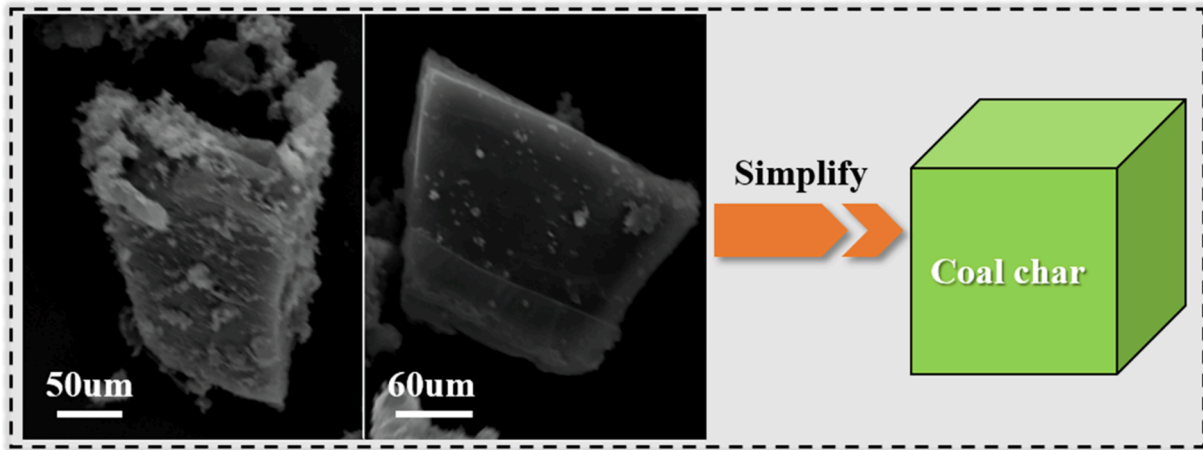


Fig. 3. Morphology characteristics and modeling simplification of coal char particles.

rotation is accompanied by the rotational friction on the particle surface. The frictional force on the particle surface is opposite to the direction of particle rotation, forming a frictional resistance torque M_f . The magnitude of this torque is proportional to the rotation angular velocity of solid particles. With the increase of particle rotation angular velocity, the frictional resistance torque continues to increase until it is equal to the thrust torque M_O induced by the gas–solid surface reactions, as shown in Fig. 2(B). The particle rotational angular velocity reaches balance.

2.2. Particle rotation speed

In this paper, the steady-state simulation is used to obtain the reaction rate distribution on particle surface during the combustion process of coal char particles. The net force and its torque on non-spherical particle are calculated by post-processing. The rotational frequency of a non-spherical particle is estimated based on the torque to particle centroid. The pressure on reacting micro-area is contributed by the gaseous reactants and products fluxes according to the momentum conversion, which is defined as

$$p_i = v_r \frac{dm'_r}{dt} + v_p \frac{dm'_p}{dt} \quad (1)$$

$$\vec{v} = \frac{dm}{\rho \cdot S \cdot \vec{n}_s \cdot dt} \quad (2)$$

here, v_r is the reactants velocity, v_p is the products velocity. The velocity is calculated by diffusion fluxes on particle surface based on the equation (2). \vec{n}_s is the normal unit vector of reacting surface. dm'_r/dt ($\text{kg}/\text{m}^2\text{s}$) is the absorption rate of gaseous reactants, dm'_p/dt ($\text{kg}/\text{m}^2\text{s}$) is the release rate of gaseous products. The mass fluxes of reactants and products to/from particle surface are obtained by steady-state simulation. The chemical reaction of solid particles is modeled in section 3.

The thrust on the i -th micro-area of the particle surface is calculated as follows:

$$\vec{F}_i = p_i A_i \vec{n}_s = \begin{bmatrix} F_{ix} \\ F_{iy} \\ F_{iz} \end{bmatrix} \quad (3)$$

where p_i is the pressure on the i -th micro-region, and A_i is the area of i -th micro-region. For the whole particle, the net thrust can be expressed as:

$$\vec{F} = \sum_i \vec{F}_i \quad (4)$$

The particle center of gravity O is at the coordinate origin $(0,0,0)$.

Therefore, the torque of the induced thrust \vec{F}_i at the i -th micro-region with centroid coordinate of (x, y, z) can be calculated by the following formula.

$$\vec{M}_O(\vec{F}_i) = \vec{r}_{Oi} \times \vec{F}_i = \begin{bmatrix} i & j & k \\ x & y & z \\ F_{ix} & F_{iy} & F_{iz} \end{bmatrix} \quad (5)$$

Thus, the net torque of all induced thrusts on the particle surface to the centroid O is integrated as follows.

$$\vec{M}_O(\vec{F}) = \sum \vec{M}_O(\vec{F}_i) = \begin{bmatrix} \sum_i M_{ix} \\ \sum_i M_{iy} \\ \sum_i M_{iz} \end{bmatrix} = \begin{bmatrix} M_x \\ M_y \\ M_z \end{bmatrix} \quad (6)$$

$$|\vec{M}_O(\vec{F})| = \sqrt{M_x^2 + M_y^2 + M_z^2} \quad (7)$$

The particles rotation is accompanied by the rotational friction on the particle surface, as illustrated in Fig. 2(B). The rotational friction torque of whole particle surface is defined as [26]:

$$M_f = \zeta \omega \quad (8)$$

here, ζ is the rotational friction coefficient and ω is the rotational angular velocity. The influence of particle rotation direction on the rotational friction coefficient is ignored. And the rotational friction coefficient of cubic particles is estimated by the formula of spherical particles [26].

$$\zeta = \pi \mu d^3 \quad (9)$$

here, d is the equivalent diameter of equal volume sphere of the cubic particle. The equivalent diameter of equal volume sphere is defined as:

$$d = \left(\frac{6}{\pi} \right)^{1/3} l \quad (10)$$

When the frictional torque formed by rotational friction is equal to the thrust torque induced by gas–solid phase reactions, the particle rotation angular velocity reaches balance.

$$|\vec{M}_O(\vec{F})| = M_f \quad (11)$$

Thus, the balanced angular velocity ω and rotational frequency f of solid particles can be calculated as follows:

$$\omega = \frac{|\vec{M}_O(\vec{F})|}{\zeta} \quad (12)$$

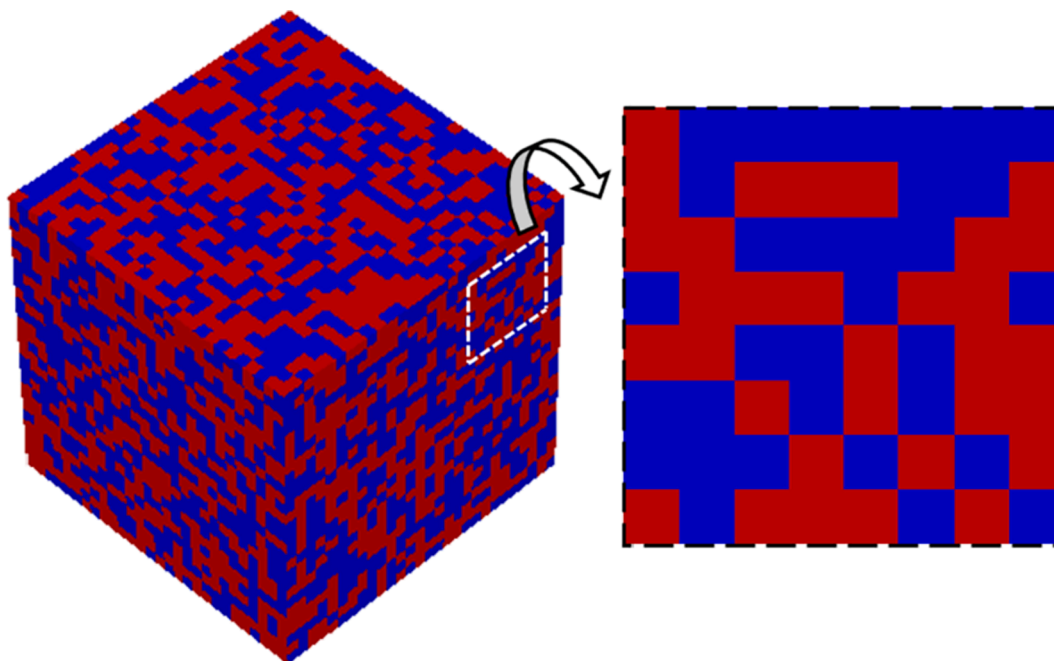


Fig. 4. Distribution of active sites on cubic particle surface and an enlarged partial schematic view; active sites (red), non-active sites (blue). (For interpretation of the references to colour in this figure legend, the reader is referred to the web version of this article.)

$$f = \omega/(2\pi) \quad (13)$$

3. Mathematic modeling

3.1. Active sites modeling

The numerical simulation for a single char particle is carried out in our study to reveal the rotational phenomenon during combustion process. Usually, the rotation phenomenon of coal particles has been widely reported [16–19] in experiments. The surface morphologies and structures of Zhongmeng (ZM) bituminous coal chars were measured by the scanning electron microscopy (SEM), as shown in Fig. 3. In this work, the coal char particle is modeled by the cube with side length of l to simplify the research and better explain the rotation mechanism of non-spherical particles, because the cube represents a simplest regular non-spherical particle. The composition of coal char particles is extreme complex. In our previous study [27], the ash aggregations with the characteristic size of 2–6 μm were randomly distributed on the char particle surface. The random distribution of ash aggregations leads to the non-uniform distribution of active sites. Based on the random distribution of ash aggregations, the active site distribution model is proposed for the cubic particle. One distribution of active sites on cubic particle surface and an enlarged partial schematic view are shown in Fig. 4. For feasibility of calculation and study, several assumptions and simplifications for modelling are introduced as follows.

1. A coal char particle consists of reactive carbon and non-reactive ash. The active area ratio is defined as the active area S_r to the whole particle surface area S .

$$a = \frac{S_r}{S} \quad (14)$$

2. The chemical reactions occur at the active sites (reactive carbon) on particle surface. The porosity of the particle is ignored to exclude the intraparticle diffusion.

3. The char particle surface is divided into many uniform square cells, as shown in Fig. 4. The active sites are the reactive carbon marked in red in the Fig. 4. The non-active sites are the non-reactive ash marked in blue.

Table 1

Reaction rates for homogeneous reactions.

Reaction	R_i (kmol/m ³ •s)	A_r	E_a (J/kmol)	β_r	ref
R1	$K_{\text{CO}}[\text{CO}][\text{H}_2\text{O}]^{0.5}[\text{O}_2]^{0.25}$	2.24×10^{12}	1.6736×10^8	0	[28]
R2	$K^f[\text{CO}][\text{H}_2\text{O}]$	2.74×10^9	8.368×10^7	0	[29]
R3	$K^b[\text{CO}_2][\text{H}_2]$	9.98×10^{10}	1.205×10^8	0	[30]

4. Each cell on cubic particle surface is a potential active site. The probability of each cell to be active site is the same, which is equal to the active area ratio a .

3.2. Chemical reactions

Based on the active-sites distribution in Fig. 4, the three homogeneous and four heterogeneous reactions are considered for char particles, written as follows:

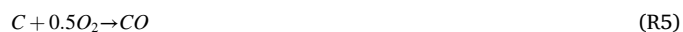


Table 2

Reactions rates for heterogeneous reactions.

Reaction	A_r	E_a (J/kmol)	β_r	ref
R4	4.605 m/(s•K)	1.751×10^8	1	[31]
R5	3.007×10^5 m/s	1.4937×10^8	0	[32]
R6	11.25 m/(s•K)	1.751×10^8	1	[31]
R7	593.83 m/(s•K)	1.4965×10^8	1	[33]



The semi-global reactions rates of three homogeneous and four heterogeneous chemical reactions are listed in Table 1 and Table 2. The catalytic effect of water vapor on CO combustion was considered [28]. The forward and backward water–gas shift reactions were used [34,35]. The rate constant for each reaction follows the Arrhenius expression:

$$k_r = A_r T^{\beta_r} e^{-E_a/RT} \quad (15)$$

where, A_r is pre-exponential factor, β_r is temperature exponent, E_a is activation energy for the reaction, and T is temperature.

3.3. Governing equation

The combustion of coal char particles is a transient reaction process with the continuous consumption of carbon. For the statistical convenience of induced thrusts and torques on particle surface, the Pseudo-steady-state [28] approach is applied for the combustion of cubic char particle. The Navier-Stokes equations coupled with the energy and species conservation equations are used to solve the flow field.

Continuity and momentum equations:

$$\nabla \cdot (\rho \vec{v}) = 0 \quad (16)$$

$$\nabla \cdot (\rho \vec{v} \vec{v}) = -\nabla p + \nabla \cdot (\vec{\tau}) \quad (17)$$

where p is the static pressure, the stress tensor $\vec{\tau}$ is given by.

$$\vec{\tau} = \mu \left[(\nabla \vec{v} + \nabla \vec{v}^T) - \frac{2}{3} \nabla \cdot \vec{v} I \right] \quad (18)$$

here, μ is the molecular viscosity, and I is the unit tensor.

The mixture material is modelled by incompressible ideal gas law:

$$\rho = \frac{p}{RT \sum_i \frac{Y_i}{M_i}} \quad (19)$$

here, R is the universal gas constant; Y_i is the mass fraction of species i ; M_i is the molecular weight of species i .

Species and energy transport equations:

$$\nabla \cdot (\rho \vec{v} Y_i) = \nabla \cdot (\rho D_{i,m} \nabla Y_i) + R_i \quad (20)$$

where R_i is the net rate of production of species i by chemical reaction, and $D_{i,m}$ is the mass diffusion coefficient for species i in the mixture.

$$R_i = M_i \sum_{r=1}^{N_R} \hat{R}_{i,r} \quad (21)$$

here, $\hat{R}_{i,r}$ is the Arrhenius molar rate of creation or destruction of species i in reaction r .

$$\nabla \cdot (\rho \vec{v} h) = \nabla \cdot (\lambda \nabla T - \vec{q}_r) - \sum_i \frac{h_i^0}{M_i} R_i \quad (22)$$

where λ is the thermal conductivity, h is the sensible enthalpy, h_i^0 is the enthalpy of formation of species i . For the radiation heat transfer, the P-1 radiation model is used [30,35], which can be expressed as follows:

$$q_r = -\frac{\nabla G}{3\alpha} \quad (23)$$

$$\nabla \cdot \left(\frac{\nabla G}{3\alpha} \right) - \alpha G + 4an^2\sigma T^4 = 0 \quad (24)$$

$$-\nabla \cdot q_r = \alpha G - 4an^2\sigma T^4 \quad (25)$$

here, α is the absorption coefficient, G is the incident radiation, n is the refractive index of the medium, and σ is the Stefan-Boltzmann constant.

The values for μ , λ , and D are calculated by kinetic theory [30]. The heat capacity of the mixture is calculated by polynomial expression.

Inward heat flux:

Based on the steady-state simulation, the particle interior is ignored [30,34]. The heat flux Q_1' of the particle inward heat transfer has been proposed and validated in our previous study [27]. It was found that the numerical particle surface temperature without the inward heat transfer is 200–300 K higher than the experimental results. The inward heat flux is estimated by the internal heat capacity and burnout time based on the combustion of single particle [36].

$$Q_1 = mc_p \Delta T \quad (26)$$

$$\Delta T = T_s - T_\infty \quad (27)$$

$$Q_1' = \frac{Q_1}{S \cdot \tau_t} = \frac{4/3\pi r^3 \rho_s c_p (T_s - T_\infty)}{4\pi r^2 \tau_t} = \frac{r \rho_s c_p (T_s - T_\infty)}{3\tau_t} \quad (28)$$

$$\tau_t = \eta \cdot \tau_b \quad (29)$$

where m is the particle mass, r is the particle radius, c_p is the specific heat capacity, ρ_s is the coal char density, 1400 kg/m³. T_s and T_∞ are the surface temperature of particle and the ambient temperature, S is the particle surface area. τ_t is the heat transfer time, estimated by the burnout time. The τ_b and η are the particle burnout time and the proportion of heat transfer time during the combustion process. According to the work of Riaza [16], the coefficient η is given as 0.105. The diffusion-controlled combustion of char particle follows the d^2 -law [36].

$$d_0^2 - d^2(t) = k_c t \quad (30)$$

$$k_c = \frac{4\rho_g Nu_D^* D}{\rho_c} \ln(1+B) \quad (31)$$

$$B = \frac{2\omega_{O_2,\infty} - \frac{v_s-1}{v_s} \omega_{CO_2,\infty}}{v_s - 1 + \frac{v_s-1}{v_s} \omega_{CO_2,\infty}} \quad (32)$$

where d is the particle diameter, $v_s = 44/12 = 3.664$, ρ_g is the gas density, ρ_c is the carbon density, D is the gas mass diffusion coefficient [37], $\omega_{O_2,\infty}$ and $\omega_{CO_2,\infty}$ are the mass fraction of O₂ and CO₂. Nu_D^* equals 2 when the char particle is pure diffusion-controlled combustion without the influence of convection.

Boundary conditions on particle surface

Species diffusion effects in the energy equation due to wall surface reactions are included in the normal species diffusion term. The heat flux of particle inward heat transfer is considered by the wall boundary conditions based on the equation (28). The convective and diffusive mass fluxes of the gas-phase species at the surface are balanced by the production/destruction rates of gas-phase species caused by surface reactions.

$$\rho_{wall} D_i \frac{\partial Y_{i,wall}}{\partial n} - \dot{m}_c Y_{i,wall} = M_{w,i} \hat{R}_{i,s} \quad (33)$$

$$\dot{m}_c = \sum_{i=1}^{N_R} M_{w,i} \hat{R}_{i,s} \quad (34)$$

where $\hat{R}_{i,s}$ (kmol/m²s) is the production rate of species i due to the surface reaction (R4-R7), \dot{m}_c is the net mass flux between the surface and the gas, the index $_{wall}$ refers to the gas side at the wall.

Simulation conditions and methods

A single cubic coal char particle was placed stationarily in the center of a 266 l × 266 l × 266 l cube flow field, where l is the side length of cubic particle. The flow field is large enough to avoid blockage effects and ensure the adequacy of gaseous reactants. The computational domain and numerical grids around particle are illustrated in Fig. 5. The boundary condition of particle surface is no slip, and the far field

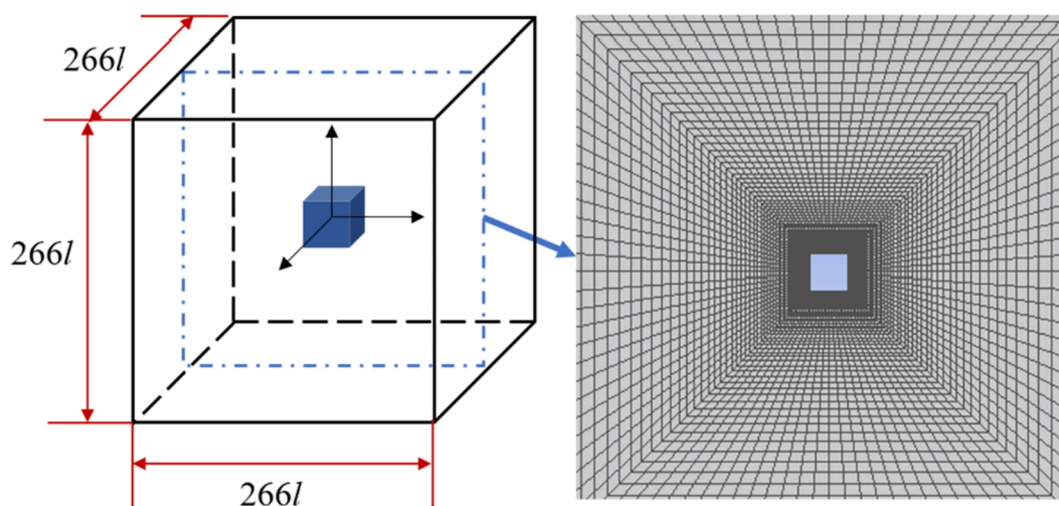


Fig. 5. Computational domain and numerical grids around particle.

Table 3
Numerical conditions.

Particle size l (μm)	Ambient temperature T_0 (K)	Operating pressure p (atm)	Air (mass fraction)		
			O ₂	N ₂	H ₂ O
150	1573	1	0.233	0.766	0.001

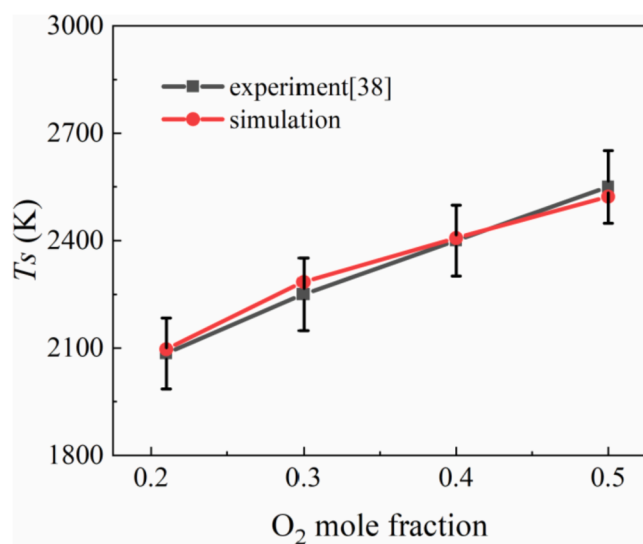


Fig. 6. Validation against experimental data [38].

boundary is the pressure outlet. In our previous work [27], we analyzed the ash distribution on particle surface by field emission scanning electron microscopy (FESEM). The characteristic size of ash aggregations was 2–6 μm . The specific size of the cell on particle surface is consistent with the characteristic size of ash aggregation. Detailed description of grid dependence can be found in the work [27]. The reaction property of each cell on particle surface is obtained by a random function based on the active site distribution model. Then, the active and inactive sites are defined by multiplying 1 or 0 by the reaction rate constant via user defined functions (UDF). The heat flux Q_l' of the inward heat transfer is added in the particle surface as the wall boundary condition. The basic numerical conditions are shown in Table 3. Char density is 1400 kg/m^3 . The governing equations were solved by the finite volume numerical algorithm based on the commercial software

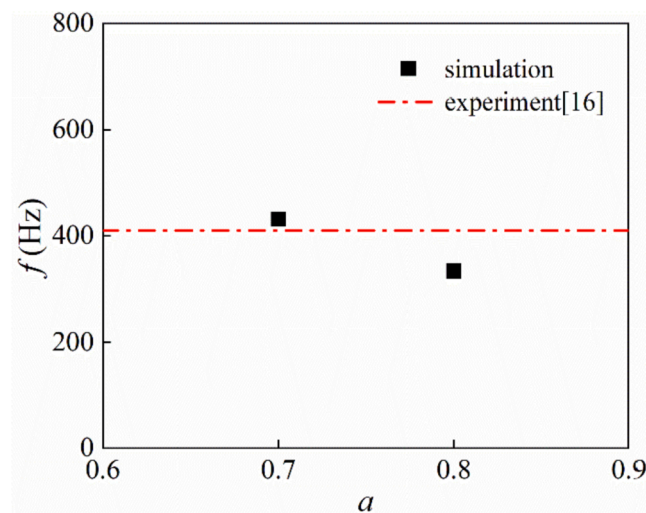


Fig. 7. The numerical validation against experiment [16] for anthracite coal particle.

Fluent. The convection terms were discretized by means of the QUICK scheme. The SIMPLE algorithm was adopted for pressure velocity coupling. The under-relaxation factors were set as 0.7.

3.4. Model validation

3.4.1. Temperature validation

In order to validate the proposed models, we compared our numerical results with the experimental data of particle temperature measured by Bejarano [38] for 90 μm particles in O₂/N₂ at 1400 K. All the model conditions were identical to Bejarano's experimental conditions. According to the equivalent diameter of equal volume sphere, the side length l of the cubic particle is 72 μm . Re was estimated to be 1. The active area ratio a used in simulation was estimated to be 0.8 based on the ultimate analysis of the coal in Bejarano's experiment. Fig. 6 presents the comparison between our numerical results and experimental results. The numerical simulation results are in good agreement with the experiments.

3.4.2. Rotation validation

The rotational frequency f of a single cubic char particle during the combustion process was simulated for validation. Riaza et al. [16]

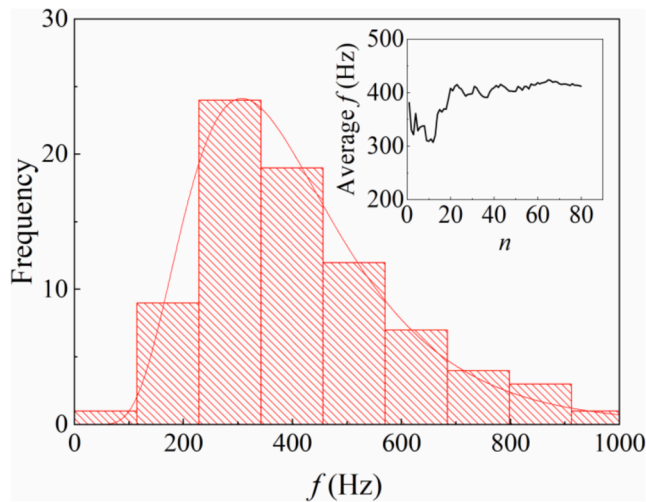


Fig. 8. Frequency histogram of rotational frequency f for different active site distributions at $a = 0.7$.

recorded the diameter periodic change of a coal particle with the combustion time in the air with the temperature of 1400 K. Coal in experiments was anthracite with particle diameter of 75–150 μm , and the fixed carbon of this anthracite was 80% by proximate analysis. We counted the rotational frequency, about 410 Hz, of anthracite coal particle for the experiments data published by Riaza [16]. For validation, the average particle size of 112 μm was used in simulation. Thus, the side length l of the cubic particle was 90 μm , according to the equivalent diameter of the equal volume sphere. The rotational frequency of a single cubic particle under $a = 0.7/0.8$ is illustrated in Fig. 7. The simulated results are basically consistent with the experiment. It should be noted that the rotational frequency in Fig. 7 is an average result. There are many active sites distributions for the same active area ratio. For different active sites distributions with the same a , the temperature and consumption rate of the particle surface are the same, but the induced thrust and rotational frequency are greatly affected. Fig. 8 shows the frequency histogram of rotational frequency f under different active sites distributions at $a = 0.7$, based on the conditions of Riaza's experiments [16]. The numerical results of rotational frequency approximately follow the logarithmic normal distribution. The induced thrust F and rotational frequency f discussed in our work are average values, which are calculated as follows.

$$F = |\bar{F}| = \frac{\sum_{i=1}^n |\vec{F}_i|}{n} \quad (35)$$

$$f = \frac{\sum_{i=1}^n f_i}{n} \quad (36)$$

here, n is the number of samples, and i is the i -th sample. As shown in the inset figure of Fig. 8, the average f tends to be constant with the increase of calculated samples n .

In the next section of results and discussion, the reaction characteristics and the influencing factors of induced thrust and rotational frequency for non-spherical particles have been analyzed.

4. Results and discussion

4.1. Particle reaction characteristics

Fig. 9 shows an active site distribution at $a = 0.7$. The active sites are randomly distributed on the cubic particle surface, because the active probability of each site is the same. The reactivity of local micro-area on the particle surface is different, as illustrated in Fig. 9. The reactivity of

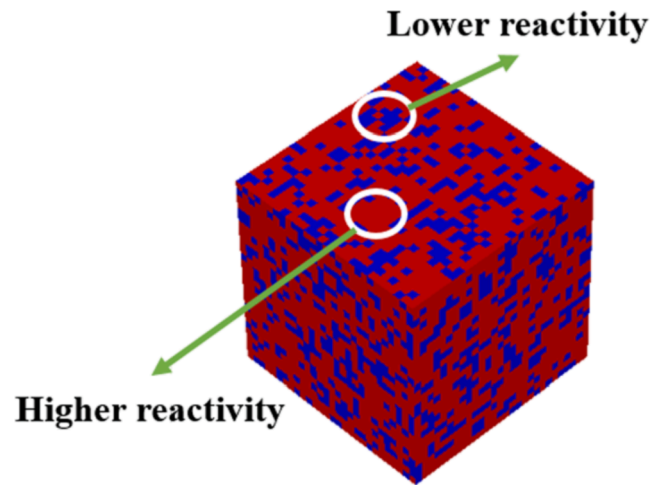


Fig. 9. Active sites distribution on particle surface; active sites (red), non-active sites (blue). (For interpretation of the references to colour in this figure legend, the reader is referred to the web version of this article.)

some micro regions is higher and that of some micro regions is lower, resulting in the non-uniform distribution of active sites. The gas–solid surface reactions take place at the active sites. Under the numerical conditions in Table 3, the reaction rate distribution of R7 on particle surface is presented in Fig. 10(A). Usually, the surface reactions rate increases with the increase of the specific surface area [24]. Compared with spherical particles, the local specific surface area of the cubic particles is related to the position, where the vertex angle $>$ edge $>$ face. The position with larger specific surface area has faster reaction rate. Therefore, the active sites with the fastest reaction rate in Fig. 10(A) is located on the vertex angle of cubic particle. The combustion of a coal char particle generates a lot of heat. The temperature of surrounding gas and the particle are increased rapidly. The temperature distribution on the particle surface is shown in Fig. 10(B). The temperature at the vertex angle is the highest, which is 200 K higher than the temperature at the face center, because the active sites at vertex angle has the fastest reaction rate.

The heterogeneous reactions consume carbon to produce gaseous products. The products are released outward at a certain speed. At plane $z = 0$, the gas velocity distribution around the cubic particle is shown in Fig. 11. The gas velocity at the edge of cube is greater, for the reaction rate on the edge of the particle is faster than the face center. The maximum velocity at this plane is about 0.45 m/s, but for the whole particle, the maximum gas released velocity can reach about 0.9 m/s at vertex angle. With the release of gaseous products from particle surface, the induced thrusts are formed. The non-uniform distribution of local active sites contributes to the uneven distribution of induced thrusts at particle surface. The net induced thrust on the whole particle and the torque of all induced thrusts to the centroid O are obtained by integration. Their numerical values are presented in the following sections.

4.2. Influence of particle active area

The proportion of active area varies with different coal rank. For a single coal particle, the proportion of active area on the particle surface is also in the process of changing with the reaction progress. Therefore, the induced thrust and the balanced rotational frequency of particles have been analyzed for different active area ratios under numerical conditions listed in Table 3. The reactive area on particle surface decreases with the decrease of the active area ratio. Thus, the reaction rate of the whole particle also reduces. Fig. 12 shows the specific carbon consumption rate for different active area ratio. The r_c increases with the increase of the active area ratio. At the same time, Fig. 13 illustrates the numerical results of the induced thrust and the rotational frequency at

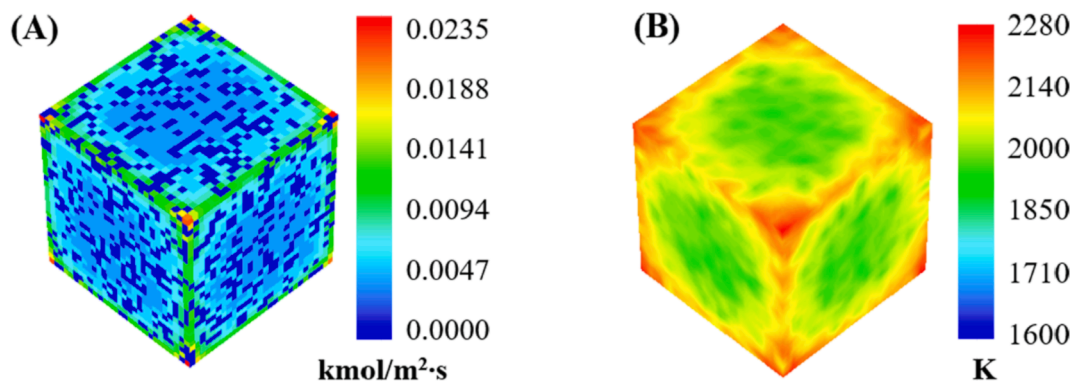


Fig. 10. (A) Reaction rate distribution of R7 on particle surface; (B) Temperature distribution on particle surface.

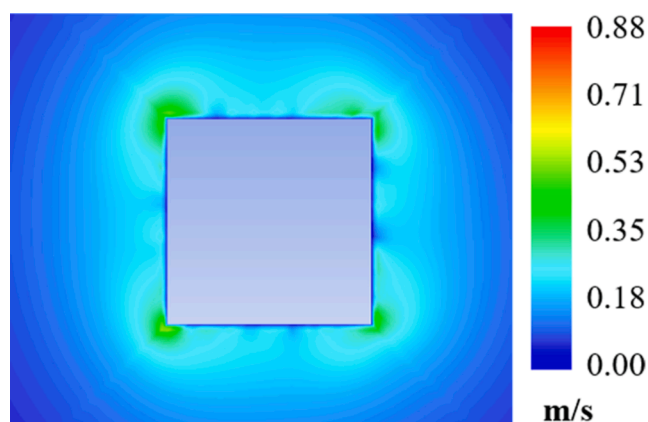


Fig. 11. Gas velocity magnitude around the particle at plane $z = 0$.

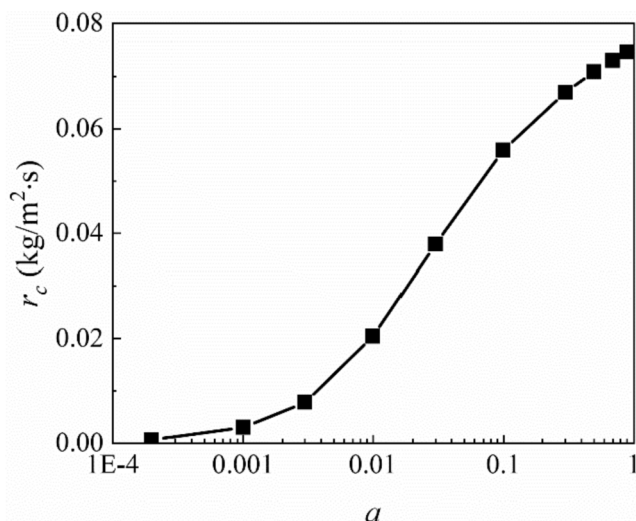


Fig. 12. Specific carbon consumption rate r_c for different active area ratio.

= 0.0002 ~ 0.9. In order to study the magnitude of induced thrust more intuitively, the thrust is compared with the particle gravity in this paper. So, Fr is defined as the ratio between the induced thrust magnitude and the particle gravity.

$$Fr = \frac{|\vec{F}|}{mg} \quad (37)$$

where, m is the particle mass.

The active area ratio has a great influence on the induced thrust and rotation of particles. As can be seen from Fig. 13, the induced thrust and rotational frequency firstly increase and then decrease with the increase of the active area ratio, which is different with the specific carbon consumption rate in Fig. 12. Because the net force on a particle is determined by the effective active area.

$$F = \sum_i^{N_e} F_i \quad (38)$$

Where, N_e is the number of effective active-sites, F_i is the force on the active-site. N_e is determined by the total number of active-sites (N_a) and the non-uniformity index (U) of the active site distribution.

$$N_e = N_a \cdot U \quad (39)$$

With the increase of the active area, the non-uniformity (U) of active site distribution decreases. The non-uniformity index is 0 for $a = 1$. Thus, the net force decreases with the increase of the active area, and the net force is 0, when $a = 1$. However, with the decrease of the active area, the number of active-sites (N_a) reduces. When $a = 0$, $N_a = 0$, so the net force is 0. Considering these two factors, the induced thrust and rotational frequency firstly increase and then decrease with the increase of the active area ratio. The changing trends of induced thrust and rotational frequency are the same. The induced thrust and rotational frequency both reaches the maximum at $a = 0.01$ – 0.03 . The maximum induced thrust is about 1.7 times that of gravity. And the maximum value of the rotational frequency is about 800 Hz.

4.3. Influence of ambient temperature

The temperature is a crucial factor for gas–solid surface reactions. The effect of temperature on particle rotation is investigated by changing the ambient temperature of numerical conditions in Table 3. Fig. 14 illustrates the induced thrust and rotational frequency for $a = 0.5 \sim 0.8$ under different air temperature. Generally, for pulverized coal, the fixed carbon content is in the range of 50% to 80%. Under $a = 0.5 \sim 0.8$, the induced thrust and rotational frequency increase with the decrease of the active area ratio, as discussed in section 4.2. As the increase of air temperature, the chemical reaction rates are enhanced. Naturally, specific carbon consumption rate r_c increases, as shown in Fig. 15. Therefore, the release rate of gaseous products increases, and the induced thrust on cubic particle is enhanced. In the range of $T_0 = 1473$ – 1873 K, the induced thrust and rotational frequency of particles increase linearly with the increase of ambient temperature, but their growth slopes decrease slightly with the increase of a . The dimensionless induced thrust Fr is about 0.3 for particles with $a = 0.5$ at $T_0 = 1473$ K. When the temperature increases by 400 K, the Fr of particles with $a = 0.5$ increases by 0.097. For particles with $a = 0.8$, Fr is about 0.17, and it increases by 0.075 when the temperature increases by 400 K. For particle rotation, the rotational frequency of particles with $a = 0.5$ increases by 51.6 Hz,

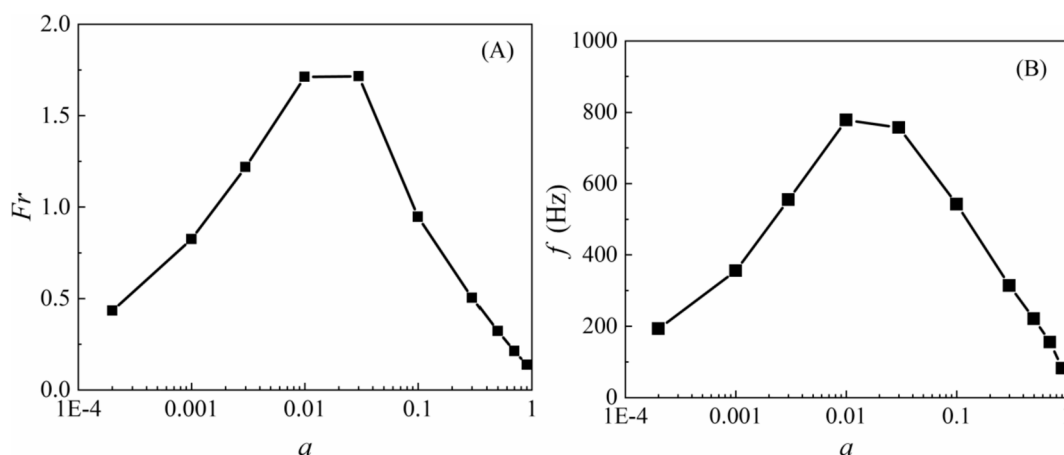


Fig. 13. (A) The induced thrust and (B) the rotational frequency of char particles for different active area ratio.

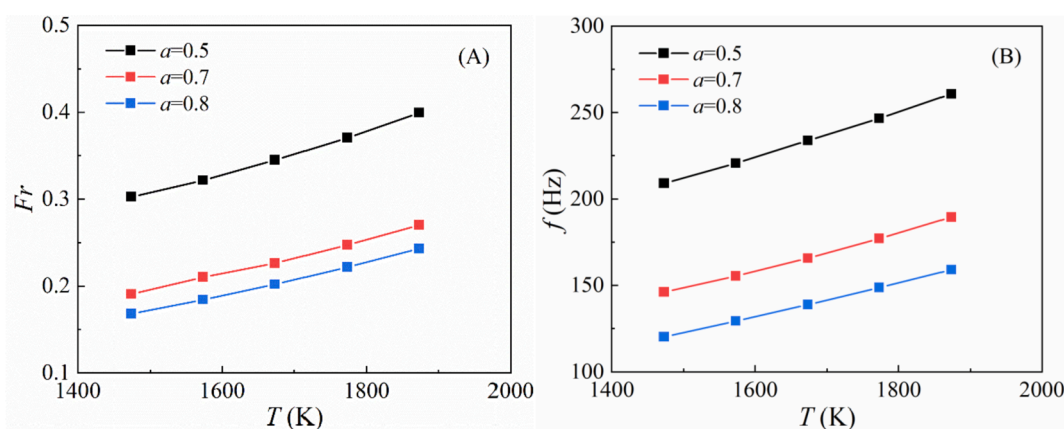


Fig. 14. (A) The induced thrust and (B) the rotational frequency of char particles for different ambient temperature.

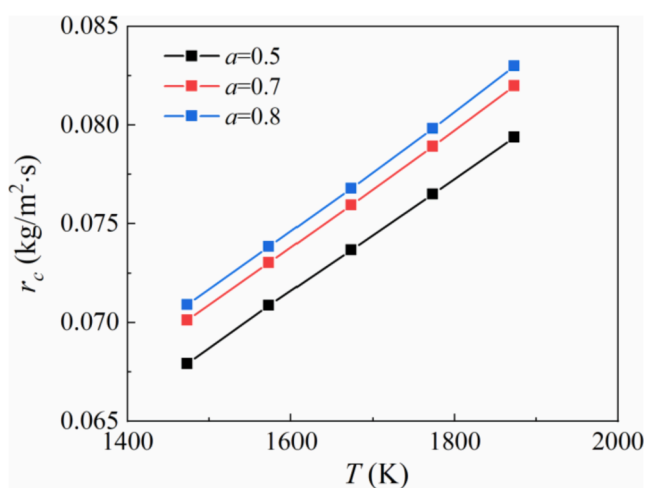


Fig. 15. Specific carbon consumption rate r_c for different ambient temperature.

while that of particles with $a = 0.8$ increases by 38.8hz.

4.4. Influence of particle size

Particle size is a vital control factor for the gas–solid phase reactions. Particle size closely affects the reaction rate and time. The influence of particle size is studied by controlling the side length of the cube in nu-

merical conditions listed in Table 3. The active area ratio is in the range of 0.5 to 0.8. Fig. 16 presents the average particle surface temperature T_s and the specific carbon consumption rate r_c for different l in log–log graph. The specific surface area of a particle is crucial to the surface reactions. Adschiri [39] found that the gasification reaction rate is proportional to the BET surface area. The specific surface area for cubic particles is defined as.

$$S' = \frac{S}{V} = \frac{6l^2}{l^3} = 6l^{-1} \quad (40)$$

The specific surface area of particles increases rapidly with the decrease of particle size. So, the reactions on particle surface are enhanced. The r_c is approximately inversely proportional to the particle size l . As shown in Fig. 16, the slope in log–log graph is 1.04, which is comparable to the 0.98 and 0.94 in references [40,41].

T_s and r_c are maximum at the side length of 60 μm . The T_s increases about 35 K for the particle of $a = 0.8$, when the side length decreases from 210 μm to 180 μm . While, it increases 96 K when l decreases from 90 μm to 60 μm . For the specific carbon consumption rate, its increase is more obvious with the decrease of particle size. r_c are between 0.05 kg/m²·s and 0.19 kg/m²·s for particles in the range of 60 μm ~ 210 μm .

Fig. 17 (log–log graph) illustrates the numerical results of Fr and f for different particle size. For 90 μm cubic particles with $a = 0.7/0.8$, the induced thrust is equivalent to particle gravity. The thrust reaches several times of the particle gravity, when the cubic particle size is 60 μm . The particle rotational frequency is as high as 1000 ~ 1500 Hz at the side length of 60 μm . For the l of 210 μm , the particle rotational frequency is in the range of 60 ~ 100 Hz. The induced thrust and rotational

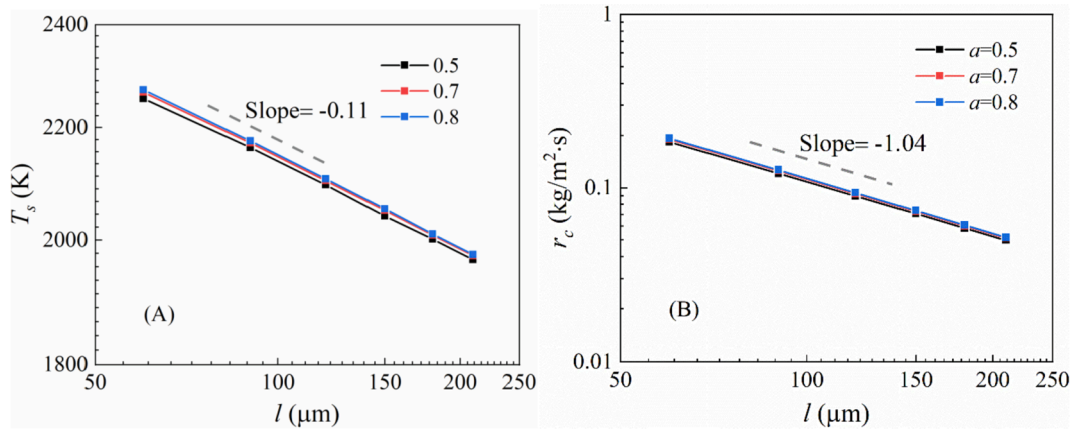


Fig. 16. (A) The average particle surface temperature T_s and (B) the specific carbon consumption rate r_c for different particle size.

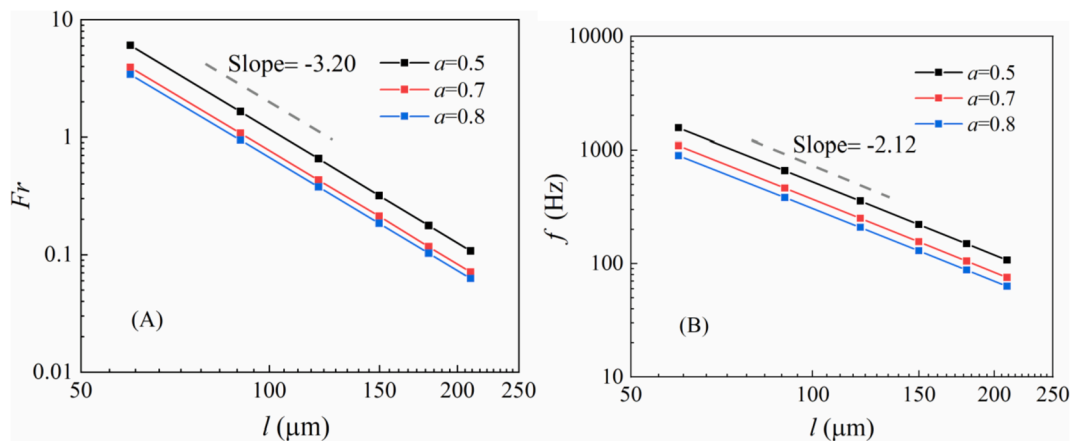


Fig. 17. (A) The induced thrust and (B) the rotational frequency of char particles with different side length.

frequency are all exponential to the particle size l . Based on the section 2, the theoretical analysis for induced thrust and rotational frequency is as follows. Fig. 16 shows the log–log graph between T_s/r_c and l . The relationship between T_s and l obtained by fitting is expressed as.

$$T_s \propto l^{-0.11} \quad (41)$$

And, the fitting result between the r_c and l is written as.

$$r_c \propto l^{-1.04} \quad (42)$$

The induced thrust on particle is contributed by the reactants and products fluxes according to the momentum conversion. The contribution of reactants and products to thrust is proportional according to the chemical equations. Based on the Eq. (1) - (4), the thrust can be defined as.

$$F = \left| \sum p_i A_i \vec{n}_s \right| \propto \frac{dm_r}{dt} v_r + \frac{dm_p}{dt} v_p \propto R_p v_p \quad (43)$$

where, m_r and m_p are the mass of the gaseous reactants and products to/from the particle surface, R_p (kg/s) is the rate of released products. According to the global reaction of carbon consumption, R_p is proportional to the rate of carbon consumption R_c (kg/s).

$$R_p \propto R_c = r_c \cdot 6l^2 \quad (44)$$

The R_p can also be related to the flow rate of gaseous products on particle surface:

$$R_p = S \rho_p v_p = 6l^2 \rho_p v_p \quad (45)$$

$$v_p \propto \frac{R_c}{6l^2 \rho_p} = \frac{r_c}{\rho_p} \quad (46)$$

here, v_p and ρ_p are the velocity and density of gaseous products.

The density of gas products follows the ideal gas law:

$$\frac{1}{\rho_p} = \frac{RT_s}{pM} \propto T_s \quad (47)$$

According to Eq. (41)-(47):

$$F \propto l^{-0.19} \quad (48)$$

Thus, the Fr can be defined as:

$$Fr = \frac{F}{mg} = \frac{F}{l^3 \rho_s g} \quad (49)$$

$$Fr \propto l^{-3.19} \quad (50)$$

According to the Eq. (5) in section 2.2, the torque of the induced thrust F can be expressed as.

$$\left| \vec{M}_o(\vec{F}) \right| \propto Fl \quad (51)$$

Thus,

$$\omega = \frac{\left| \vec{M}_o(\vec{F}) \right|}{\zeta} \propto \frac{Fl}{\mu l^3} \quad (52)$$

In our numerical results, the fitting curve between viscosity μ and

Table 4

Comparison between the theoretical results and numerical results.

	Theoretical result	Numerical result
Fr	$Fr_{\text{ocl}}^{-3.19}$	$Fr_{\text{ocl}}^{-3.20}$
f	$f_{\text{ocl}}^{-2.12}$	$f_{\text{ocl}}^{-2.12}$

particle size l is as follows:

$$\mu\alpha l^{-0.07} \quad (53)$$

Thus,

$$f = \frac{\omega}{2\pi} \alpha \frac{F}{\mu l^2} \alpha l^{-2.12} \quad (54)$$

At the same time, the numerical results of Fr and f for different particle size are illustrated in Fig. 17 (log–log graph). The direct fitting equations of Fr and f at $a = 0.5$ are as follows:

$$Fr = 3.01 \times 10^6 \times l^{-3.20} \quad (55)$$

$$f = 4.90 \times 10^6 \times l^{-2.12} \quad (56)$$

The comparison of theoretical and numerical results of Fr and f is listed in the Table 4. The theoretical results are in agreement with the numerical results. The above theoretical analysis qualitatively reveals the mechanism of non-spherical particles rotation during the combustion process.

5. Conclusion

The rotation characteristics of non-spherical particles have been analyzed based on the non-uniform distribution of active sites on the particle surface. The thrusts on the particle surface are induced by the gas–solid phase reactions. The induced thrust on different micro regions changes with the local reactivity. Thus, non-spherical particles rotate under the uneven induced thrust. The rotation model has been verified by the rotational frequency of anthracite coal char particles during combustion process. Numerical simulation results are basically consistent with the experimental results. Reaction characteristics of cubic coal char particles have been investigated. The induced thrust and the rotational frequency of particles have been analyzed for different active area ratio, gas temperatures and particle sizes. The numerical results show that the rotation velocity first increases and then decreases with the increase of the active area, and it reaches the maximum at the active area ratio of 0.01 ~ 0.03. Surface reactions rates are strengthened with the increase of ambient temperature. The induced thrust increases with the increase of reactions rate. Therefore, the induced thrust and rotation velocity of particles increase with the increase of ambient temperature. As the particle size decreases from 210 μm to 60 μm , the rotational frequency increases significantly. When l is 60 μm , the rotational frequency can reach 1000 Hz. This paper reveals the rotation mechanism of non-spherical particles in gas–solid phase reactions. It provides a basis for particle motion modeling in fluid-particle reaction process.

CRediT authorship contribution statement

Shengyu Zhou: Investigation, Data curation, Writing – original draft. **Zhongjie Shen:** Methodology, Supervision. **Qinfeng Liang:** Formal analysis. **Jianliang Xu:** Methodology, Software, Supervision, Writing – review & editing. **Zhenghua Dai:** Formal analysis. **Haifeng Liu:** Conceptualization, Methodology, Supervision.

Declaration of Competing Interest

The authors declare that they have no known competing financial interests or personal relationships that could have appeared to influence

the work reported in this paper.

Acknowledgement

This work was supported by the National Natural Science Foundation of China [Grant number 21878082].

References

- [1] Chen L, Yong SZ, Ghoniem AF. Oxy-fuel combustion of pulverized coal: characterization, fundamentals, stabilization and CFD modeling. *Prog Energy Combust Sci* 2012;38(2):156–214.
- [2] Li L, Duan L, Yang Z, Zhao C. Pressurized oxy-fuel combustion characteristics of single coal particle in a visualized fluidized bed combustor. *Combust Flame* 2020; 211:218–28.
- [3] Khatami R, Levendis YA. An overview of coal rank influence on ignition and combustion phenomena at the particle level. *Combust Flame* 2016;164:22–34.
- [4] Higman C, Tam S. Advances in coal gasification, hydrogenation, and gas treating for the production of chemicals and fuels. *Chem Rev* 2014;114(3):1673–708.
- [5] Ma K, Deng J, Wang G, Zhou Q, Xu J. Utilization and impacts of hydrogen in the ironmaking processes: a review from lab-scale basics to industrial practices. *Int J Hydrogen Energy* 2021;46(52):26646–64.
- [6] Hu G, Dam-Johansen K, Wedel S, Hansen JP. Decomposition and oxidation of pyrite. *Prog Energy Combust Sci* 2006;32(3):295–314.
- [7] Lv W, Yu D, Wu J, Zhang L, Xu M. The chemical role of CO₂ in pyrite thermal decomposition. *P Combust Inst* 2015;35(3):3637–44.
- [8] Liu R, Jing N, Song Y, Sun W. *Sep Purif Technol* 2021;276:119425.
- [9] Theofanidis SA, Batchu R, Galvita VV, Poelman H, Marin GB. Carbon gasification from Fe-Ni catalysts after methane dry reforming. *Appl Catal B* 2016;185(15): 42–55.
- [10] Zhou J, Zhao J, Zhang J, Zhang T, Ye M, Liu Z. Regeneration of catalysts deactivated by coke deposition: a review. *Chin J Catal* 2020;41(7):1048–61.
- [11] Wu X, Wang Q, Luo Z, Fang M, Cen K. Experimental study of particle rotation characteristics with high-speed digital imaging system. *Powder Technol* 2008;181 (1):21–30.
- [12] Kajishima T. Influence of particle rotation on the interaction between particle clusters and particle-induced turbulence. *Int J Heat Fluid Flow* 2004;25(5):721–8.
- [13] Gao X, Li Y, Garcia-Perez M, Wu H. Roles of inherent fine included mineral particles in the emission of PM10 during pulverized coal combustion. *Energy Fuel* 2012;26(11):6783–91.
- [14] Xu M, Yu D, Yao H, Liu X, Qiao Y. Coal combustion-generated aerosols: Formation and properties. *P Combust Inst* 2011;33(1):1681–97.
- [15] Sun Y, Zheng S. Influence of particle rotation and partial irradiation on the particle heating up process. *Int Commun Heat Mass* 2020;119:104892.
- [16] Riaza J, Khatami R, Levendis YA, Álvarez L, Gil MV, Pevida C, et al. Single particle ignition and combustion of anthracite, semi-anthracite and bituminous coals in air and simulated oxy-fuel conditions. *Combust Flame* 2014;161(4):1096–108.
- [17] Bai X, Lu G, Bennet T, Sarroza A, Eastwick C, Liu H, et al. Combustion behavior profiling of single pulverized coal particles in a drop tube furnace through high-speed imaging and image analysis. *Exp Therm Fluid Sci* 2017;85:322–30.
- [18] Lee H, Choi S. Motion of single pulverized coal particles in a hot gas flow field. *Combust Flame* 2016;169:63–71.
- [19] Kang SW, Sarofim AF, Beér JM. Particle rotation in coal combustion statistical experimental and theoretical studies. *Symp (Int) Combust* 1989;22(1):145–53.
- [20] Liu M, Shen Z, Liang Q, Liu H. Particle fluctuating motions induced by gas-solid phase reaction. *Chem Eng J* 2020;388:124348.
- [21] Xu K, Hu S, Su S, Xu C, Sun L, Shuai C, et al. Study on char surface active sites and their relationship to gasification reactivity. *Energy Fuel* 2013;27(1):118–25.
- [22] Li J, Li Z, Yang Y, Duan Y, Xu J, Gao R. Examination of CO, CO₂ and active sites formation during isothermal pyrolysis of coal at low temperatures. *Energy* 2019; 185:28–38.
- [23] Li J, Li Z, Yang Y, Zhang X. Study on the generation of active sites during low-temperature pyrolysis of coal and its influence on coal spontaneous combustion. *Fuel* 2019;241:283–96.
- [24] Zhang R, Chen Y, Lei K, Liu D. The effects of specific surface area and ash on char gasification mechanisms in the mixture of H₂O, CO₂, H₂ and CO. *Fuel* 2017;209: 109–16.
- [25] Roberts MJ, Everson RC, Domazetis G, Neomagus HWJP, Jones JM, Van Sittert CGCE, et al. Density functional theory molecular modelling and experimental particle kinetics for CO₂–char gasification. *Carbon* 2015;93:295–314.
- [26] Hu CM, Zwanzig R. Rotational friction coefficients for spheroids with the slipping boundary condition. *J Chem Phys* 1974;60(11):4354–7.
- [27] Zhou S, Shen Z, Liang Q, Xu J, Dai Z, Liu H. Numerical simulation analysis of the induced thrust on a char particle in reaction process. *AIChE J* 2022.
- [28] Turns SR. An introduction to combustion: concepts and applications. New York: McGraw-Hill; 2000.
- [29] Jones WP, Lindstedt RP. Global reaction schemes for hydrocarbon combustion. *Combust Flame* 1988;73(3):233–49.
- [30] Richter A, Nikrityuk PA, Kestel M. Numerical investigation of a chemically reacting carbon particle moving in a Hot O₂/CO₂ atmosphere. *Ind Eng Chem Res* 2013;52 (16):5815–24.
- [31] Libby PA, Blake TR. Burning carbon particles in the presence of water vapor. *Combust Flame* 1981;41:123–47.

- [32] Caram HS, Amundson NR. Diffusion and reaction in a stagnant boundary layer about a carbon particle. *Ind Eng Chem Fundam* 1977;16(2):171–81.
- [33] Date AW, editor. *Introduction to Computational Fluid Dynamics*. Cambridge University Press; 2005.
- [34] Nikrityuk PA, Gräbner M, Kestel M, Meyer B. Numerical study of the influence of heterogeneous kinetics on the carbon consumption by oxidation of a single coal particle. *Fuel* 2013;114:88–98.
- [35] Richter A, Nikrityuk PA, Meyer B. Three-dimensional calculation of a chemically reacting porous particle moving in a hot O₂/CO₂ atmosphere. *Int J Heat Mass Transfer* 2015;83:244–58.
- [36] Wang J, Li J, Liu X. *Combustion*. Beijing: Beijing Institute of Technology Press; 2017.
- [37] Perry RH. *Perry's Chemical Engineers' Handbook*—Sixth Edition. New York: McGraw-Hill Book Company; 1984.
- [38] Bejarano PA, Leventis YA. Single-coal-particle combustion in O₂/N₂ and O₂/CO₂ environments. *Combust Flame* 2008;153(1–2):270–87.
- [39] Adschiri T, Furusawa T. Relation between CO₂-reactivity of coal char and BET surface area. *Fuel* 1986;65(7):927–31.
- [40] Xue Z, Guo Q, Gong Y, Xu J, Yu G. Numerical study of a reacting single coal char particle with different pore structures moving in a hot O₂/CO₂ atmosphere. *Fuel* 2017;206:381–9.
- [41] Stauch R, Maas U. Transient detailed numerical simulation of the combustion of carbon particles. *Int J Heat Mass Transfer* 2009;52(19–20):4584–91.